Research Square

Preprints are preliminary reports that have not undergone peer review.
They should not be considered conclusive, used to inform clinical practice,
or referenced by the media as validated information.

Unlocking electron transfer across carbon overlayers via single-atom engineered built-in electric field for industrial water purification

Yafei Zhao

yafeizhao@ustc.edu.cn

Department of Chemistry, iChEM (Collaborative Innovation Center of Chemistry for Energy Materials), University of Science and Technology of China, Hefei 230026. https://orcid.org/0000-0001-5098-7753

Tianran Sheng

university of science and technology of china https://orcid.org/0000-0003-1831-4377

Xing-En Lin

University of Science and Technology of China

Gang Zhao

University of Science and Technology of China

Ruoyan Wei

Institute of Biological Information Processing (IBI-3), Bioelectronics, Forschungszentrum Jülich

Xiangyu Shu

Biomass Oligosaccharides Engineering Technology Research Center of Anhui Province, Fuyang Normal University

Cheng Qian

Department of Chemistry, iChEM (Collaborative Innovation Center of Chemistry for Energy Materials), University of Science and Technology of China

Zhen Zhang

Biomass Oligosaccharides Engineering Technology Research Center of Anhui Province, Fuyang Normal University

Liangquan Sheng

Biomass Oligosaccharides Engineering Technology Research Center of Anhui Province, Fuyang Normal University

Yude Su

University of Science and Technology of China https://orcid.org/0000-0002-3553-9458

Article

Keywords:

Posted Date: November 9th, 2026

DOI: https://doi.org/10.21203/rs.3.rs-11520806/v1

License: This work is licensed under a Creative Commons Attribution 4.0 International License.
Read Full License

Additional Declarations: There is **NO** Competing Interest.

Unlocking electron transfer across carbon overlayers via single-atom engineered built-in electric field for industrial water purification

Tianran Sheng,[1,2,7] Xingen Lin,[1,6,7] Gang Zhao,[1,3] Ruoyan Wei,[1,5] Xiangyu Shu,[4] Cheng Qian[1,2], Zhen Zhang,[4] Liangquan Sheng,[4]* Yude Su,[1,3]* Yafei Zhao[1,2]**

[1]State Key Laboratory of Precision and Intelligent Chemistry, School of Chemistry and Materials Science, University of Science and Technology of China, Hefei, Anhui 230026, China

[2]Deep Space Exploration Laboratory, University of Science and Technology of China, Hefei, Anhui 230026, China

[3]School of Nano Science and Technology, State Key Laboratory of Bioinspired Interfacial Materials Science, Suzhou Institute for Advanced Research, University of Science and Technology of China, Suzhou, Jiangsu 215123, China

[4]Biomass Oligosaccharides Engineering Technology Research Center of Anhui Province, Fuyang Normal University, Fuyang, Anhui 236037, China

[5]Institute of Biological Information Processing (IBI-3), Bioelectronics, Forschungszentrum Jü lich, 52425 Jülich, Germany

[6]Southern Sichuan Gas District, PetroChina Southwest Oil & Gasfield Company, Luzhou, Sichuan 646001, China

[7]These authors contributed equally to this work.

*Correspondence to: yafeizhao@ustc.edu.cn; suyude@ustc.edu.cn; shenglq2015@163.com.

Precisely regulating active-sites structures and charge transfer kinetics is crucial for developing high-performance catalysts, yet achieving their synergy remains challenging. Herein, we anchor atomically dispersed cobalt electronic coupling nodes into ultrathin N-doped carbon overlayers (4–5 atomic layers thick) with metallic nanoparticles inside (M@Co$_1$, M = Co$_2$P, Co, Ni or Cu). As revealed by characterization and theoretical calculations, the isolated Co sites mediate interlayer electron transfer between the confined nanoparticles and outermost catalytic interfaces. The extended d-orbital states of single-cobalt atoms establish a

built-in electric field and enable work-function matching in hybrid nanostructures. Efficient electron mobility facilitates product desorption and decreases the charge-transfer resistance toward reactants to 19.8% of that in the Co_1-deficient counterpart. Accordingly, $Co_2P@Co_1$ exhibits excellent industrial water purification ability via peroxymonosulfate activation, achieving ≥99% phenol removal in 90 s at a low catalyst dosage. It also shows environmental tolerance in real matrices, such as residual organic solvents and inorganic ions.

Metal-supported catalysts underpin numerous industrial reactions[1–4] such as propane dehydrogenation[5,6], CO_2 reduction[7,8] and Fischer–Tropsch synthesis[9], owing to their abundant free electrons and surface-active sites. Unlike ionic or covalent solids, where local coordination environments can be independently engineered, electrons in metals are delocalized. Site-specific modulation is inherently difficult because perturbing an individual active site inevitably propagates through neighboring metal atoms, resulting in collective electronic responses[10,11]. As a result, the adsorption energies of reactants and key intermediates remain subject to linear scaling relations (LSRs), yet in the ideal catalyst: one that activates reactants well, but binds intermediates relatively weakly[12,13]. Their hyperactive surfaces often sacrifice reaction selectivity, including over-hydrogenation[14], deep oxidation[15], or excessive bond cleavage[16]. Besides that, the thermodynamic instability of metal nanoparticles (NPs) causes size growth and/or metal ion dissolution during long-term operation[17,18].

Recent advances in ultrathin carbon overlayers have validated that they can actively regulate the electronic structures of encapsulated metals beyond serving as protective barriers[19-21]. For instance, graphene nanopockets enable efficient confinement of Pt NPs, reducing noble-metal consumption while enhancing catalytic activity and stability in proton exchange membrane fuel cells[22,23]. Yet this strategy introduces a new dilemma. Studies on carbon-layer-dependent electronic interactions have revealed that increasing the number of carbon layers gradually

suppresses interfacial electron transfer and metal–surface electronic coupling[24]. Therefore, catalytic reactions involving encapsulated metals rely on mass transport processes, such as ionic or molecular diffusion, rather than direct electron-transfer. The intrinsic interlayer electron transport barrier in stacked graphene is hard to break[25,26]. Overcoming the electronic isolation imposed by carbon overlayers and achieving site-specific, efficient electron communication across hybrid interfaces is crucial.

Here, we report a class of conductive NPs encapsulated beneath 4–5 atomic-layer-thick nitrogen-doped carbon overlayers functionalized with atomically dispersed Co sites (M@Co_1, M = Co_2P, Co, Ni, Cu). Among them, Co_2P@Co_1 delivers exceptional peroxymonosulfate (PMS) activation with a rate constant of 1972 min^{-1} M^{-1}, and enables rapid degradation of diverse organic pollutants via an electron-transfer mechanism. The heterostructure also exhibits remarkable stability in complex and real aqueous matrices. More importantly, we uncover a long-range (radial, core to shell) electron-transfer pathway driven by work-function integration, where Co sites mediate electron flow from inner NPs to the surface single-Co sites across the overlayers. The rapid electron supply promotes the cleavage of the S-O bonds and the desorption of the reaction intermediate, thereby optimizing the reaction pathway. Removing these Co sites weakens the metal-support interaction (MSI). Such a synergistic interplay is rarely captured in previous idealized monolayer models that primarily emphasize local coordination activation[27]. This work offers new insights into engineering hierarchical catalytic interfaces that reconcile selective adsorption with effective electron transport.

Cobalt single-atom engineered electron transfer across carbon overlayers

For constructing integrated nanoparticle–overlayer architectures, we developed a general two-step strategy to synthesize a series of catalysts on nitrogen-doped carbon (NC) supports. Conductive nanoparticles like metal or metal phosphide (M; M= Co_2P, Co, Ni, Cu) are

encapsulated within multilayer carbon shells enriched with nitrogen vacancies (N_v), while atomically dispersed cobalt sites (Co_1) are anchored in the overlayers, yielding the configuration denoted as M@Co_1 (Fig. 1d, Supplementary Figs. 1,2,10,11,29a). Bright-field HRTEM (BF-HRTEM) and aberration-corrected HAADF-STEM images combined with elemental mapping directly visualizes the isolated Co_1 species decorating the external carbon shells (thickness 1.0–1.5 nm) without detectable aggregation (Figs. 1a–c, Supplementary Figs. 3,4), confirming the spatial separation between encapsulated NPs and surface single cobalt atoms. To decouple the intrinsic nanoparticle–overlayer synergy, control samples containing only nanoparticles (Co_2P/NC), only cobalt single-atoms (Co_1/NC) or pristine Co_2P NPs were prepared (Supplementary Figs. 5–8, 16–20).

To elucidate interfacial charge redistribution across the carbon overlayer, spatially resolved electron energy-loss spectroscopy (EELS) was performed at distinct regions. The Co L-edge at the NP core in Co_2P@Co_1 (site 1, grey point) exhibits a positive energy shift relative to the particle region in Co_2P/NC (site 3, red point), while also differing from the cobalt single-atom only region (site 2, blue point), indicating electron depletion from the Co_2P core (Figs. 1e–g). By comparison, Co_2P/NC exhibits a Co L-edge nearly identical to that of Co_2P NPs, showing that carbon encapsulation alone does not induce appreciable charge depletion. Complementary C K-edge EELS collected from the carbon directly above the NP, at the particle edge, and in regions distant from the NPs reveals spatial variations in the carbon near-edge electronic structure (Figs. 1h, Supplementary Fig. 9). The relative π* contribution associated with the sp^2-conjugated carbon framework is higher in the NP-associated region and gradually decreases toward regions distant from the NPs, suggesting a decay of the electronic modulation induced by the NP–carbon interface. Such evolution may arise from the stronger interfacial coupling and reconstructed π-electronic states near the encapsulated NPs, while the perturbation progressively weakens away

from the interface. Combined with the Co L-edge shift, these results reveal spatially separated interfacial charge redistribution between the inner NPs and the conjugated carbon overlayer, generating an electronically polarized interface that underlies the formation of a built-in electric field.

We next designed an oxygen-activation Raman probe under solvent-free gas–solid conditions to track the formation of oxygenated species in ambient air using a high-energy 532 nm laser as the external excitation source. Interestingly, only $Co_2P@Co_1$ exhibits a distinct Raman band centered at 672 cm^{-1}, assigned to Co–O species[28], while no oxygen-derived signal appears for either Co_2P/NC or Co_1/NC (Fig. 1i, j). The absence of this feature indicates that oxygen activation does not originate from isolated structural components alone, but rather from the synergistic electronic interaction within the Co_2P–carbon–Co_1 architecture. Considering the intrinsic oxygen adsorption capability of isolated Co sites, the formation of Co–O species indicates that Co_1 sites serve as oxygen-binding centers, while the adjacent Co_2P cores may act as electron donors. Therefore, these results reveal a directional electron-transfer pathway from Co_2P NPs to atomically dispersed Co_1 sites across the carbon overlayers, ultimately enabling O_2 adsorption and activation. Consistent with the follow-up PMS activation results, this finding further verifies that Co_1 incorporation establishes an efficient charge-transfer channel for regulating oxygen-involved catalytic processes. Similar phenomena can also be observed in other metal NPs-based systems (Supplementary Figs. 21b,22), highlighting the general applicability of the interfacial electronic coupling strategy.

X-ray absorption spectroscopy (XAS) further demonstrates that such radial charge migration is accompanied by electronic and structural coupling. In the XANES spectra (Fig. 1k, Supplementary Fig. 13), the absorption edge of $Co_2P@Co_1$ nearly overlaps with that of Co_2P NP and lies between metallic Co and CoO, indicating that cobalt predominantly remains in a low-

valence state characteristic of the Co_2P environment[29]. However, the pre-edge peaks evolution reveals that the introduction of Co_1 gradually change the coordination environment of Co species from tetrahedral to octahedral structure, accompanied by modulation of the Co *d*-orbital configuration. Moreover, the increased white-line intensity in $Co_2P@Co_1$ reflects a higher apparent oxidation state associated with the incorporation of Co_1. Notably, the originally well-separated peaks of white-line become broadened and more continuous, indicative of orbital hybridization across the NP–overlayer interface. EXAFS analysis corroborates this interfacial reconstruction. Compared with Co_2P NP, $Co_2P@Co_1$ displays shortened Co–Co (~2.1 Å) and Co–P (~1.8 Å) bond lengths together with reduced coordination numbers, particularly for Co–Co interactions (Fig. 1l, Supplementary Figs. 12,14,15 and Supplementary Table 1). These changes imply the disruption of Co–Co network by the surrounding carbon–nitrogen overlayer and the development of compressive strain at the interface. Such strain-induced lattice contraction promotes electronic delocalization and accelerates charge-transfer kinetics. Collectively, these structural and spectroscopic results exhibit that encapsulated NPs and outermost Co_1 sites are electronically interconnected, forming a coupled interface that provides a favorable pathway for enhanced catalytic activity.

Electron transfer accelerates PMS activation

The interfacial coupling between conductive NPs and the single-atom-decorated carbon–nitrogen overlayer markedly alters the catalytic behavior of the active centers. We selected peroxymonosulfate (PMS) activation as a model reaction and employed phenol degradation as a representative probe. Under identical Co_1 site densities, catalytic performance is closely correlated with charge-transfer kinetics: materials with faster interfacial electron transport exhibit

higher reaction rates in our non-radical system. This therefore provides a well-defined platform to research long-range electronic regulation and interfacial coupling effects (Fig. 2a).

The reaction follows apparent first-order kinetics. Benefitting from the large specific surface area and nitrogen vacancies, the metal-free catalyst (NC) has the intrinsic ability toward phenolic degradation (Supplementary Figs. 21a,38 and Supplementary Table 5). The similar degradation ability of Co_2P/NC and NC, together with no observable activity of Co_2P NPs, suggests that the catalytic sites in the absence of Co_1 are mainly associated with N-doped carbon (Supplementary Fig. 23). In contrast, $Co_2P@Co_1$ exhibits an apparent rate constant (k) 2.6 and 6.2 times higher than those of Co_1/NC and Co_2P/NC, respectively (Fig. 2b). Similar behavior is also observed with other conductive NPs (Co, Ni, Cu) (Fig. 2c). Notably, the normalized k is nearly twice that of the latest reported transition-metal-based PMS activation catalysts under comparable conditions (Fig. 2d and Supplementary Table 9). When only isolated Co_1 sites are introduced in NC, the appropriate enhancement indicates that Co_1 improves catalytic activity by tuning adsorption geometries and binding strengths of reaction intermediates, with the effect remaining limited to localized chemisorption processes as literatures reported[30,31]. However, the coexistence of Co_1 and Co_2P NPs with a strongly coupled architecture induces a distinct kinetic advantage. Chronoamperometric measurements reveal that upon successive addition of reactive species, $Co_2P@Co_1$ exhibits the most significant transient current perturbation and the highest steady-state current among all electrodes. This behavior indicates an enhanced faradaic process, suggesting accelerated interfacial electron transfer kinetics and efficient activation of the reactants. In the meantime, the open-circuit potential (OCP) response shows minimal variation, whereas the bare electrode displays the largest potential shift. This change implies the rapid charge-transfer interaction with PMS, leading to its consumption in electrolyte with a lower equilibrium potential (Fig. 2e, Supplementary Fig. 35). The pronounced enhancement cannot be

attributed to a simple additive effect of active sites, but instead arises from strong metal–support interactions (MSI) between the Co_1-contained overlayers and NPs[32]. Within this cooperative system, Co_1 sites function not only as catalytic centers but also as electronic mediators, facilitating interfacial charge transfer on N-doped carbon framework. As a result, this design alleviates the intrinsically limitations associated with sluggish electron-transfer kinetics in carbon-based catalysts that often used in advanced oxidation processes (AOP).

In diffusion-controlled radical or singlet oxygen systems, even small amounts of organic solvents, such as alcohols commonly present in industrial effluents, can act as radical scavengers and severely suppress activity[33]. The present $Co_2P@Co_1$ maintains high degradation efficiency in various organic solvents (10 vol%) (Fig. 2g), highlighting its resistance to interference due to the electron-transfer mechnism of PMS activation. This also enables rapid and broad-spectrum degradation of antibiotics, dyes and phenolic pollutants (Fig. 2f, Supplementary Tables 6,7), while exhibiting exceptional environmental robustness. The catalyst sustains stable operation across high ionic strengths, a wide pH and temperature window, and in complex real-water matrices including tap water and river water (Fig. 2g, Supplementary Figs. 25–27). When pharmaceutical wastewater was diluted 100-fold and treated with $Co_2P@Co_1$ for 5 minutes, the total organic carbon (TOC) removal reached 71%, which could be further improved to 93% under sufficient PMS dosage (Fig. 2h, Supplementary Table 8). The catalyst exhibited a flux of 275 L m^{-2} h^{-1} in the flow-through reaction system, maintaining stable performance over 12 h with a degradation efficiency above 90% (Fig. 2i, Supplementary Fig. 24). A significant amount of bubble formation was observed, which may be attributed to the generation of singlet oxygen, molecular oxygen or CO_2 gas. Meanwhile, the treated effluent exhibited markedly reduced ecological toxicity, as evidenced by the growth of *E. coli*, underscoring the practical applicability

of this electronic-regulation strategy for advanced wastewater remediation (Supplementary Fig. 28).

To elucidate the origin of the accelerated reaction kinetics, radical-quenching experiments were conducted to identify the reactive species involved (Fig. 3b, Supplementary Fig. 31). The addition of methanol (MeOH) or tert-butanol (TBA) (scavengers for hydroxyl radicals (•OH) and sulfate radicals ($SO_4^{\bullet-}$), respectively) showed negligible influence on the *k* value across Co_2P@Co_1, Co_1/NC, Co_2P/NC and NC systems, indicating that these radical pathways do not dominate the reaction. In contrast, furfuryl alcohol (FFA), a selective quencher for singlet oxygen ($^1O_2$)[34], moderately suppressed activity, with the inhibition being most obvious in the cobalt-free NC system. This observation suggests that pristine NC primarily operates through a non-radical oxidation pathway mediated by $^1O_2$.

Upon introduction of Co_1 sites, the interfacial charge-transfer resistance between the catalyst and electrolyte decreases, and an electron-transfer-dominated oxidation mechanism progressively becomes predominant, as reflected by the attenuated inhibitory effect of FFA. Further incorporation of Co_2P NPs amplifies this behavior (Fig. 3c, Supplementary Table 4). The *quasi*-rectangular cyclic voltammetry (CV) profile, together with the larger enclosed area, suggests enhanced capacitive behavior with minimal polarization, showing rapid charge–discharge capability and facilitated ion diffusion within the hybrid architecture (Supplementary Figs. 36,37). The strong electronic coupling at the overlayer–NP interface in Co_2P@Co_1 improves directional electron transport from pollutants to PMS. The addition of *p*-benzoquinone (a superoxide scavenger, *p*-BQ) produces minimal inhibition at low concentration but substantial suppression at higher concentration[34]. This concentration-dependent effect is likely associated with adsorption or electron-acceptor competition, given the structural similarity between *p*-BQ

and phenolic substrates. Electron paramagnetic resonance (EPR) spectroscopy corroborates these findings. All four catalysts generate $^1O_2$ signals, whereas no detectable •OH or SO_4•$^-$ signals are observed. Notably, only Co_2P@Co_1 exhibits a progressively intensifying OOH• signal during the reaction (Fig. 3d, Supplementary Figs. 29b, 30). Control experiments conducted under an inert atmosphere confirm that the oxygen source of OOH• originates from PMS rather than dissolved O_2 (Supplementary Figs. 33,34). The emergence of OOH• is attributed to altered PMS adsorption configurations on Co_1 site[35-37]. These results indicate that the encapsulated Co_2P NPs not only enhance bulk and interfacial charge-transfer capability but also reshape the coordination environment and orbital configuration of surface Co_1 sites, thereby enabling more efficient PMS activation.

X-ray photoelectron spectroscopy (XPS) analysis reveals pyridinic and graphitic nitrogen as the dominant species, with pyridinic nitrogen acting as a π-acceptor and graphitic nitrogen showing weaker electronic modulation (Supplementary Fig. 17). But the lower degradation efficiency of electron-rich substrates contradicts a π–π stacking-dominated mechanism (Fig. 2e). Instead, substrates bearing stronger electron-donating groups, associated with weaker phenolic acidity and more stable O–H bonds, exhibit the lower electron density over the entire molecule and are degraded more rapidly. It suggests that adsorption is primarily mediated by hydrogen bonding between nitrogen sites in the catalyst and phenolic hydroxyl groups (N···H–O), rather than π–π stacking. Then, high-performance liquid chromatography–mass spectrometry (HPLC–MS) was employed to trace the degradation pathway of phenol. Fragmentation analysis indicates a dominant ring-opening pathway. Following electron abstraction by the catalyst, oxidative rearrangement of the phenolic carbon and adjacent carbon atoms forms unstable *ortho*-quinone intermediates, which subsequently undergo C–C bond cleavage (Fig. 3a, Supplementary Fig. 39),

yielding acetic acid and ultimately CO_2. Minor dimeric products arising from direct oxidative transfer polymerization (DOTP) are also detected[38].

Collectively, these results demonstrate that the system does not proceed via a single non-radical pathway. Instead, an electron-transfer mechanism predominates. Through the synergistic Co_1–Co_2P interfacial interaction, electrons are directionally injected into PMS, generating OOH• species, while pollutants subsequently replenish electrons to the catalyst (Fig. 3e). In NC regions, oxidation proceeds via $^1O_2$ formed in situ and diffusing through solution. The addition of DMSO does not significantly affect degradation kinetics[39], excluding the involvement of high-valent metal–oxo species (Supplementary Fig. 32). Comparison with Co_1/NC further highlights that the NPs in support functions as an active electronic regulator that modulates both the electronic structure of single-atom centers and electron-transport dynamics.

Mechanism of catalytic performance

The above experimental observations establish a pronounced synergy in $Co_2P@Co_1$ between Co_2P NPs and single Co sites, manifested as reduced charge-transfer resistance and long-range electronic modulation of surface Co_1 sites. To rationalize these effects at the atomic level, density functional theory (DFT) calculations were performed using a multilayer carbon–nitrogen framework encapsulating a Co_2P NP. This model explicitly captures the spatial separation between the NP core and surface single atoms, enabling analysis of long-range electronic coupling that is inaccessible to conventional monolayer graphene-based models.

Charge density distributions under identical excitation conditions (Figs. 4a,c, Supplementary Fig. 46) reveal that, relative to Co_2P/NC, the Co_1 sites in $Co_2P@Co_1$ exhibit more spatially extended *d*-electron density. These delocalized electronic states enhance orbital's overlap across adjacent graphitic layers, establishing a continuous electronic transport pathway from encapsulated NP to the external surface. In contrast, carbon overlayers without single cobalt

atom incorporation exhibit weak electronic coupling, effectively trapping charge carriers within the NP core. Interestingly, Co_1/NC, despite possessing stronger interlayer electronic coupling, displays a higher charge-transfer resistance than Co_2P@Co_1. This apparent inconsistency is resolved by work function, which reflects the energetic barrier for electron emission to vacuum level. Although transition-metal atom promotes interlayer coupling via conjugated π bonds (Co 3*d*-C 2*p*), they also induce localized charge redistribution within the carbon framework, generating interfacial dipoles with spatially separated positive and negative charge regions[40]. This internal electrostatic polarization suppresses electron escape from the surface by driving electron migration toward electron-deficient regions, yielding the highest work function among the investigated systems (Supplementary Fig. 44). Calculated work functions further elucidate the role of interfacial coupling (Figs. 4b, d–f, Supplementary Fig. 45). In the absence of Co_1, Co_2P/NC and NC exhibit nearly identical work functions, indicating that encapsulated NPs alone do not appreciably modulate the electronic emission characteristics of the multi-carbon framework. By contrast, the work function of Co_2P@Co_1 shifts toward that of Co_2P NPs, signifying the formation of an electronically integrated system. This coupling enables surface Co_1 sites to efficiently relay electrons originating from the NP core, while preserving the intrinsic orbital specificity and adsorption selectivity of SAC.

Beyond facilitating long-range electron transport, NP incorporation reconfigures the electronic structure of surface Co_1 sites. Orbital-projected analyses show that in Co_1/NC, PMS adsorption is dominated by interaction between the Co dz^2 orbital and oxygen atoms through an anti-σ configuration, which is highly directional. Electron injection requires precise orbital alignment, while steric hindrance limits its efficiency. In Co_2P@Co_1, however, the dominant interaction involves the Co *d*xz orbital via an anti-π configuration, which is energetically more accessible and spatially less constrained (Supplementary Figs. 40–42). This σ-to-π transition

reflects a reorientation of the Co *d*-orbital and enhances electronic delocalization at the catalyst–reactant interface. As a consequence, the adsorption geometry of PMS is altered from a relatively flat configuration on Co_1/NC to a near-vertical orientation on $Co_2P@Co_1$, facilitating S–O bond cleavage and reducing OOH• desorption constraints. Consistently, the calculated interfacial charge-transfer amount increases from 0.058 e^- in Co_1/NC to 0.073 e^- in $Co_2P@Co_1$ (Fig. 4g, Supplementary Fig. 43), indicating strengthened donor–acceptor interactions and more efficient electron injection into PMS. This enhanced coupling favors PMS reduction to generate OOH• and SO_3^{2-} species, whereas in the absence of Co_1 the charge-transfer direction reverses, promoting PMS self-coupling and $^1O_2$ formation[41]. Reaction energy profiles further show that $Co_2P@Co_1$ binds more strongly to the partially negatively charged S–O moiety of PMS (Fig. 4h, Supplementary Figs. 47–50), owing to both orbital reconfiguration and reinforced electrostatic interactions at the Co_1 site. The strengthened electronic coupling significantly lowers the activation barrier from transition state TS1 to $*SO_3^{2-}$ + OOH•, accounting for the experimentally observed acceleration of PMS activation. Density-of-states (DOS) analysis corroborates the formation of a continuous electronic coupling channel at the interface (Fig. 4f). While Co_2P/NC exhibits limited and spatially separated P–C hybridization, $Co_2P@Co_1$ displays overlaps between the *d*-orbitals of Co_1 and Co in Co_2P, accompanied by additional Co_1–P hybridization. Due to the relatively electron-deficient nature of Co_1 compared with Co and P in Co_2P, electrons preferentially migrate from the NP core to surface single-atom sites. This directional electronic distribution provides the fundamental driving force for sustained electron supply during catalysis, thereby unifying the theoretical predictions with the observed enhancement in catalytic kinetics.

In summary, we report a high-performance catalytic architecture for wastewater treatment over state-of-the-art systems. This improvement arises from a strongly coupled interface between single-atom overlayers and nanoparticle, which induces synergistic electronic modulation at Co_1

sites. Substituting the inner NP with Co, Ni or Cu displays similar trends. This generality confirms that the activity amplification does not originate from the intrinsic property of a specific metal species. We demonstrate that the conductive NP with low work function acts as an internal electron reservoir embedded within a carbon–nitrogen framework, remotely tuning the electronic states of surface single-atom centers without direct coordination. Then, electrons are efficiently transmitted to the outermost Co_1 sites on the overlayers and subsequently injected into PMS via an energetically favorable anti-π orbital pathway, thereby overcoming kinetic limitations in PMS activation. The radial electron channel achieves rapid charge transfer with efficient molecular adsorption. Overall, this study highlights that optimizing catalytic performance requires the deliberate construction of strong interfacial electronic synergistic effect rather than merely increasing the density of active sites. Moreover, the multi-layer theoretical model construction has established a more realistic representation of the long-range electronic cooperative effects, rather than the ideal coordination effects.

Methods

Preparation of Co_2P@Co_1, Co_1/NC and NC: Typically, P-123 (0.5 g), and TPP (0.375 g) were dissolved in 24 mL of ethanol at 80 °C. After that, ground melamine (5 g) and $Co(NO_3)_2{\cdot}6H_2O$ (0.032 g) were then added sequentially, and the resulting mixture was stirred for 1 h. While the reaction mixture was still hot, the flask was removed from the heating source and 1 mL of deionized water was added. Then the mixture was concentrated by rotary evaporation under reduced pressure (0.065 MPa) at 55 °C for 1 h, until no liquid was visible. Evaporation was then continued for an additional 0.5–1 h, taking care not to overdry the sample, as excessive drying leads to hardening of the material and diminishes the structure-directing effect of P-123. The

precursor was obtained as a white or pale white–green solid. Noted that if it turns purple, the catalytic performance is poor. More water should be added or the evaporation temperature should be lowered. The solid was then placed in a tube furnace and calcined under flowing Ar with the flow rate at about 20 mL min^{-1}. The temperature was increased to 800 °C at a heating rate of 10 °C min^{-1} and held for 4 h, then cooled to room temperature over 4.5 h. The resulting product was collected, weighed at least 26 mg, and gently crushed without vigorous grinding. If liquid or gas is sucked back due to too slow air flow, a buffer bottle should be installed. Adjusting the $Co(NO_3)_2{\cdot}6H_2O$ to 0.014 g will obtain Co_1/NC. Without adding cobalt, NC is obtained.[42]

Preparation of Co_1/NC+Co_2P, Co@Co_1, Ni@Co_1, Cu@Co_1, Co/NC, Ni/NC, Cu/NC: The precursor of Co_1/NC was placed in a tube furnace and calcined under flowing Ar with the flow rate at about 20 mL min^{-1}. The temperature was increased to 660 °C at a heating rate of 10 °C min^{-1} and held for 2.5 h, then cooled to room temperature over 3.9 h. The resulting product was collected. Then, a certain amount of NP in hexane solution was diluted to 4 mL and the obtained solid was dispersed into it. Drying by rotary evaporation. The mixture was placed in a tube furnace and calcined under flowing Ar with the flow rate at about 20 mL min^{-1}. The temperature was increased to 800 °C at a heating rate of 10 °C min^{-1} and held for 2 h, then cooled to room temperature over 4.5 h. At this point, we can obtain Co_1/NC+Co_2P, Co@Co_1, Ni@Co_1. When we use the precursor of NC, we obtain Co/NC, Ni/NC. For the low melting point of Cu NPs, the second step cannot be carried out at 800 °C. We set the first step of calcination at 800 °C, and the second step at 660 °C. We can get the Cu@Co_1 and Cu/NC.

Characterization

The catalyst morphology was examined by HR-TEM, high-angle annular dark-field scanning transmission electron microscopy, selected area electron diffraction and energy-dispersive X-ray

spectroscopy were performed on a Themis Z TEM electron microscope at an accelerating voltage of 300 kV. Electron energy loss spectroscopy was conducted using a Quantum ER/965P detector. The material compositions and metal valence states were analyzed by XPS (ESCALAB 250Xi, Thermo Fisher Scientific Inc., USA) with an Al *K*α radiation source. The binding energies of all peaks were referenced to the C*1s* line (285.0 eV). The crystalline phases were characterized by a powder X-ray diffraction instrument (MiniFlex II, Rigaku) with CuK_{α} ($\lambda = 1.5418$ Å) radiation (cathode voltage 30 kV, current 15 mA). Raman spectra were recorded on a laser microscopic confocal Raman spectrometer (Renishaw inVia) at 532 nm. Electrochemical experiment data were collected using a CHI660F workstation. The X-ray absorption spectroscopy for Co K edge was measured at beamline BL01C at the National Synchrotron Radiation Research Center (NSRRC, Hsinchu, Taiwan, China). Elemental analysis was performed using a Vario EL cube elemental analyzer (Elementar Analysensysteme GmbH, Germany). The combustion tube was maintained at 1000 °C, while the reduction tube was set to 800 °C. Detection was carried out using a thermal conductivity detector (TCD) at 59.7 °C. Inductively coupled plasma optical emission spectroscopy (ICP–OES) measurements were conducted on an Optima™ 8000 instrument (PerkinElmer, USA) according to the manufacturer's standard operating conditions.

Pollutant Degradation Experiments

All the batch experiments for pollutant degradation were conducted in 100-mL beakers at 25 ± 1 °C under mechanical stirring, and were repeated at least twice. Initially, 1.2 mg of the catalyst was added to 40.0 mL of a phenol solution (or other contaminants) at 20 mg/L, followed by 10 min of ultrasonic dispersion to ensure uniform suspension. Subsequently, 1 mL of PMS (12 g/L) stock solution was introduced to start the reaction. Samples were collected at regular intervals, immediately treated with 0.05 M $Na_2S_2O_3$ methanol solution to stop the reaction, then filtered

through a 0.22 μm Nylon-6 filter. For the ROS quenching and anti-interference experiment, after adding the catalyst to the solution and ultrasonic it for ten minutes, we add scavengers and other speices. The packed-bed column reactor was loaded with a mixture of catalyst (120 mg) and melamine foam (diameters of 5 cm, thickness of 3 cm). The river water was collected from Qiyu River in Fuyang, China, filtered through 0.22-μm membrane to remove the suspended solids, and spiked with a certain amount of PhOH.

Electrochemical characterizations

They were conducted on a conventional three-electrode system. A glassy carbon electrode (3 mm diameter, GC), a Pt wire and a Ag/AgCl/KCl (saturated) electrode as the working, counter and reference electrode, respectively. A catalyst ink was prepared by dispersing 5 mg of the catalyst in 0.48 mL isopropanol, followed by the addition of 0.02 mL of 5 wt% Nafion solution. The mixture was ultrasonicated to obtain a homogeneous dispersion. GC was modified by drop-casting 0.01 mL of the ink onto the GC surface and drying to form a catalyst layer. This drop-casting and drying procedure was repeated three times to ensure uniform coverage. Electrochemical measurements were conducted in 0.1 M Na_2SO_4 electrolyte at 25 °C. The open-circuit potential (OCP) was monitored as a function of time under open-circuit conditions to evaluate the spontaneous potential evolution of the electrode/electrolyte interface. Cyclic voltammetry (CV) was performed in the potential window of 0.1–0.3 V versus the reference electrode for three cycles, with scan rates as specified in the measurement settings. Chronoamperometry (CA) was carried out by applying a constant potential equal to the OCP measured immediately prior to the CA test, and the resulting current–time response was recorded. Electrochemical impedance spectroscopy (EIS) was performed at the OCP with an AC

perturbation amplitude of 10 mV over a frequency range of 3 MHz to 1 Hz. The impedance spectra were fitted using ZView software.

Computational methods

Density functional theory (DFT) calculations were performed to investigate the electronic structure, density of states, work function and charge redistribution of the studied systems. Structural optimization, total energy and electronic structure calculations were carried out using the QuickStep module implemented in the CP2K package, which employs a hybrid Gaussian and plane-wave (GPW) approach for efficient and accurate electronic structure calculations. The generalized gradient approximation (GGA) with the Perdew–Burke–Ernzerhof (PBE) functional was used to describe exchange–correlation interactions. The Goedecker–Teter–Hutter (GTH) pseudopotentials were employed to represent the core electrons, together with the DZVP-MOLOPT-SR-GTH. The self-consistent field (SCF) convergence criterion was set to 1.0×10^{-5} eV per atom. The work function and electrostatic potential distributions were further evaluated using the DMol³ module in the Materials Studio package. Exchange–correlation effects were also treated within the GGA-PBE functional framework. The plane-wave ultrasoft pseudopotential was adopted to describe electron–ion interactions. The energy cutoff was set to 300 eV, and the SCF convergence tolerance was fixed at 1.0×10^{-5} eV per atom. Structural optimization was considered converged when the energy change, maximum force, maximum stress and maximum atomic displacement were less than 5.0×10^{-5} eV per atom, 0.05 eV $Å^{-1}$, 0.1 GPa, and 0.002 Å, respectively. The Brillouin zone was sampled using a $2 \times 1 \times 2$ Monkhorst–Pack k-point mesh for bulk calculations. To analyze the charge redistribution during the interaction process, charge density difference calculations were performed and visualized using the Multiwfn wavefunction

analysis package, which allows detailed analysis of electronic structure and charge transfer characteristics.

Data availability

The main data that support the plots in this paper and other finding of this study are available within the article and its Supplementary Information. Extra data are available from the corresponding author upon reasonable request.

References

1 Guo, Y., Wang, M., Zhu, Q., Xiao, D. & Ma, D. Ensemble effect for single-atom, small cluster and nanoparticle catalysts. *Nat. Catal.* **5**, 766-776 (2022).

2 Li, X. *et al.* Advances in heterogeneous single-cluster catalysis. *Nat. Rev. Chem.* **7**, 754-767 (2023).

3 Ding, J., Liu, L., Yang, H. B., Zhang, T. & Liu, B. Integrative catalytic pairs driving complex chemical reactions. *Nat. Rev. Chem.* **9**, 826-840 (2025).

4 Feidenhans'l, A. A. *et al.* Precious Metal Free Hydrogen Evolution Catalyst Design and Application. *Chem. Rev.* **124**, 5617-5667 (2024).

5 Yan, H. *et al.* Tandem In_2O_3-Pt/Al_2O_3 catalyst for coupling of propane dehydrogenation to selective H_2 combustion. *Science* **371**, 1257-1260 (2021).

6 Chen, S. *et al.* Defective TiO_x overlayers catalyze propane dehydrogenation promoted by base metals. *Science* **385**, 295-300 (2024).

7 Matsubu, J. C. *et al.* Adsorbate-mediated strong metal–support interactions in oxide-supported Rh catalysts. *Nat. Chem.* **9**, 120-127 (2017).

8 Yang, Y. *et al.* Operando studies reveal active Cu nanograins for CO_2 electroreduction. *Nature* **614**, 262-269 (2023).

9 Li, J. *et al.* Integrated tuneable synthesis of liquid fuels via Fischer–Tropsch technology. *Nat. Catal.* **1**, 787-793 (2018).

10 Nørskov, J. K., Abild-Pedersen, F., Studt, F. & Bligaard, T. Density functional theory in surface chemistry and catalysis. *Proc. Natl. Acad. Sci. U. S. A.* **108**, 937-943 (2011).

11 Saini, S., Halldin Stenlid, J. & Abild-Pedersen, F. Electronic structure factors and the importance of adsorbate effects in chemisorption on surface alloys. *npj Comput. Mater.* **8** (2022).

12 Wang, P. *et al.* Breaking scaling relations to achieve low-temperature ammonia synthesis through LiH-mediated nitrogen transfer and hydrogenation. *Nat. Chem.* **9**, 64-70 (2017).

13 Pérez-Ramírez, J. & López, N. Strategies to break linear scaling relationships. *Nat. Catal.* **2**, 971-976 (2019).

14 Zhang, L., Zhou, M., Wang, A. & Zhang, T. Selective Hydrogenation over Supported Metal Catalysts: From Nanoparticles to Single Atoms. *Chem. Rev.* **120**, 683-733 (2020).

15 Ishida, T., Murayama, T., Taketoshi, A. & Haruta, M. Importance of Size and Contact Structure of Gold Nanoparticles for the Genesis of Unique Catalytic Processes. *Chem. Rev.* **120**, 464-525 (2020).

16 Khodakov, A. Y., Chu, W. & Fongarland, P. Advances in the development of novel cobalt Fischer− Tropsch catalysts for synthesis of long-chain hydrocarbons and clean fuels. *Chem. Rev.* **107**, 1692-1744 (2007).

17 Bordet, A. & Leitner, W. Metal Nanoparticles Immobilized on Molecularly Modified Surfaces: Versatile Catalytic Systems for Controlled Hydrogenation and Hydrogenolysis. *Acc. Chem. Res.* **54**, 2144-2157 (2021).

18 Wang, T. *et al.* Nature of metal-support interaction for metal catalysts on oxide supports. *Science* **386**, 915-920 (2024).

19 Guo, K., Bao, L., Yu, Z. & Lu, X. Carbon encapsulated nanoparticles: materials science and energy applications. *Chem. Soc. Rev.* **53**, 11100-11164 (2024).

20 Jin, Z. *et al.* Nanoconfined supersaturated reactors for efficient CO_2-to-ethanol electroreduction. *Nat. Catal.* (2026). https://doi.org/10.1038/s41929-026-01601-z

21 Gao, L. *et al.* Radial nanochannel-array carbon enables high-performance intermetallic fuel cell catalysts. *Nat. Nanotechnol.* (2026). https://doi.org/10.1038/s41565-026-02244-8

22 Zhao, Z. *et al.* Graphene-nanopocket-encaged PtCo nanocatalysts for highly durable fuel cell operation under demanding ultralow-Pt-loading conditions. *Nat. Nanotechnol.* **17**, 968-975 (2022).

23 Liu, Z. *et al.* Pt catalyst protected by graphene nanopockets enables lifetimes of over 200,000 h for heavy-duty fuel cell applications. *Nat. Nanotechnol.* **20**, 807-814 (2025).

24 Hu, K. *et al.* Catalytic activity of graphene-covered non-noble metals governed by proton penetration in electrochemical hydrogen evolution reaction. *Nat. Commun.* **12**, 203 (2021).

25 Berashevich, J. & Chakraborty, T. Interlayer repulsion and decoupling effects in stacked turbostratic graphene flakes. *Phys. Rev. B* **84**, 033403 (2011).

26 Chae, D. H., Zhang, D., Huang, X. & von Klitzing, K. Electronic transport in two stacked graphene monolayers. *Nano Lett.* **12**, 3905-3908 (2012).

27 Wan, Y. *et al.* Single-Atom Supported Catalysts and Beyond. *Adv. Mater.* **37**, e2504518 (2025).

28 Li, H., Sun, C., Zhao, Y., Xu, X. & Yu, H. Facile synthesis of recyclable $Co_3O_4/Co(OH)_2$/RGO ternary heterostructures with synergistic effect for photocatalysis. *J. Nanopart. Res.* **20**, 279 (2018).

29 Zhao, G. *et al.* A Bifunctional Fibrous Scaffold Implanted with Amorphous Co_2P as both Cathodic and Anodic Stabilizer for High-Performance Li horizontal line S Batteries. *Adv. Sci.* **12**, e2501153 (2025).

30 Meng, Y. *et al.* Nanoconfinement steers nonradical pathway transition in single atom fenton-like catalysis for improving oxidant utilization. *Nat. Commun.* **15**, 5314 (2024).

31 Zhu, Z. S. *et al.* Atomic-Level Engineered Cobalt Catalysts for Fenton-Like Reactions: Synergy of Single Atom Metal Sites and Nonmetal-Bonded Functionalities. *Adv. Mater.* **36**, 2401454 (2024).

32 van Deelen, T. W., Hernández Mejía, C. & de Jong, K. P. Control of metal-support interactions in heterogeneous catalysts to enhance activity and selectivity. *Nat. Catal.* **2**, 955-970 (2019).

33 Wang, Y. *et al.* Carbonaceous materials in structural dimensions for advanced oxidation processes. *Chem. Soc. Rev.* **54**, 2436-2482 (2025).

34 Gu, C. H. *et al.* Ultrafast Water Purification by Template-Free Nanoconfined Catalysts Derived from Municipal Sludge. *Angew. Chem. Int. Ed.* **64**, e202423629 (2025).

35 Khiem, T. C. *et al.* Electron transfer-mediated enhancement of superoxide radical generation in fenton-like process: Key role of oxygen vacancy-regulated local electron density of cobalt sites. *Appl. Catal. B-Environ.* **343**, 123490 (2024).

36 Li, M. *et al.* Innovative asymmetric CoSA-N-$Ti_3C_2T_x$ catalysis: unleashing superoxide radicals for rapid self-coupling removal of phenolic pollutant. *Angew. Chem. Int. Ed.* **64**, e202502307 (2025).

37 Li, Y., Zhang, D., Wang, P., Qu, J. & Zhan, S. Superoxide radicals mediated by high-spin Fe catalysis for organic wastewater treatment. *Proc. Natl. Acad. Sci. U.S.A.* **121**, e2407012121 (2024).

38 Zhang, Y. J. *et al.* Simultaneous nanocatalytic surface activation of pollutants and oxidants for highly efficient water decontamination. *Nat. Commun.* **13**, 3005 (2022).

39 Zong, Y. *et al.* Unraveling the Overlooked Involvement of High-Valent Cobalt-Oxo Species Generated from the Cobalt(II)-Activated Peroxymonosulfate Process. *Environ. Sci. Technol.* **54**, 16231-16239 (2020).

40 Teng, Z. *et al.* Atomically dispersed low-valent Au boosts photocatalytic hydroxyl radical production. *Nat. Chem.* **16**, 1250-1260 (2024).

41 Gu, C. H. *et al.* Tuning electronic structure of metal-free dual-site catalyst enables exclusive singlet oxygen production and in-situ utilization. *Nat. Commun.* **15**, 5771 (2024).

42 Guo, Y. *et al.* Co_2P–CoN Double Active Centers Confined in N-Doped Carbon Nanotube: Heterostructural Engineering for Trifunctional Catalysis toward HER, ORR, OER, and Zn–Air Batteries Driven Water Splitting. *Adv. Funct. Mater.* **28**, 1805641 (2018).

Acknowledgments

This work was supported by National Natural Science Foundation of China (22275181), Chinese Academy of Sciences Hundred Talents Program (KJ2490007002), Research Startup Funds of the University of Science and Technology of China (KY2490000003) and Horizontal Cooperation Project of Fuyang Municipal Government – Fuyang Normal University (SXHZ202206). We thank the Instruments Center for Physical Science, University of Science and Technology of China, especially Airong Feng and Shengquan Fu, for the help in characterizations and Yingying Guo, formerly studied in Zhengzhou University, for assistance with catalyst synthesis.

Author Contributions

T.S., Y.Z. conceived and designed the experiments. X.S., T.S. and L.S. performed the experiments. X.L., G.Z., Y.S., R.W., Z.Z. and C.Q. analyzed the data. G.Z. analyzed and fitted the XAFS data.

Competing interests

The authors declare no competing interests.

Figures and captions

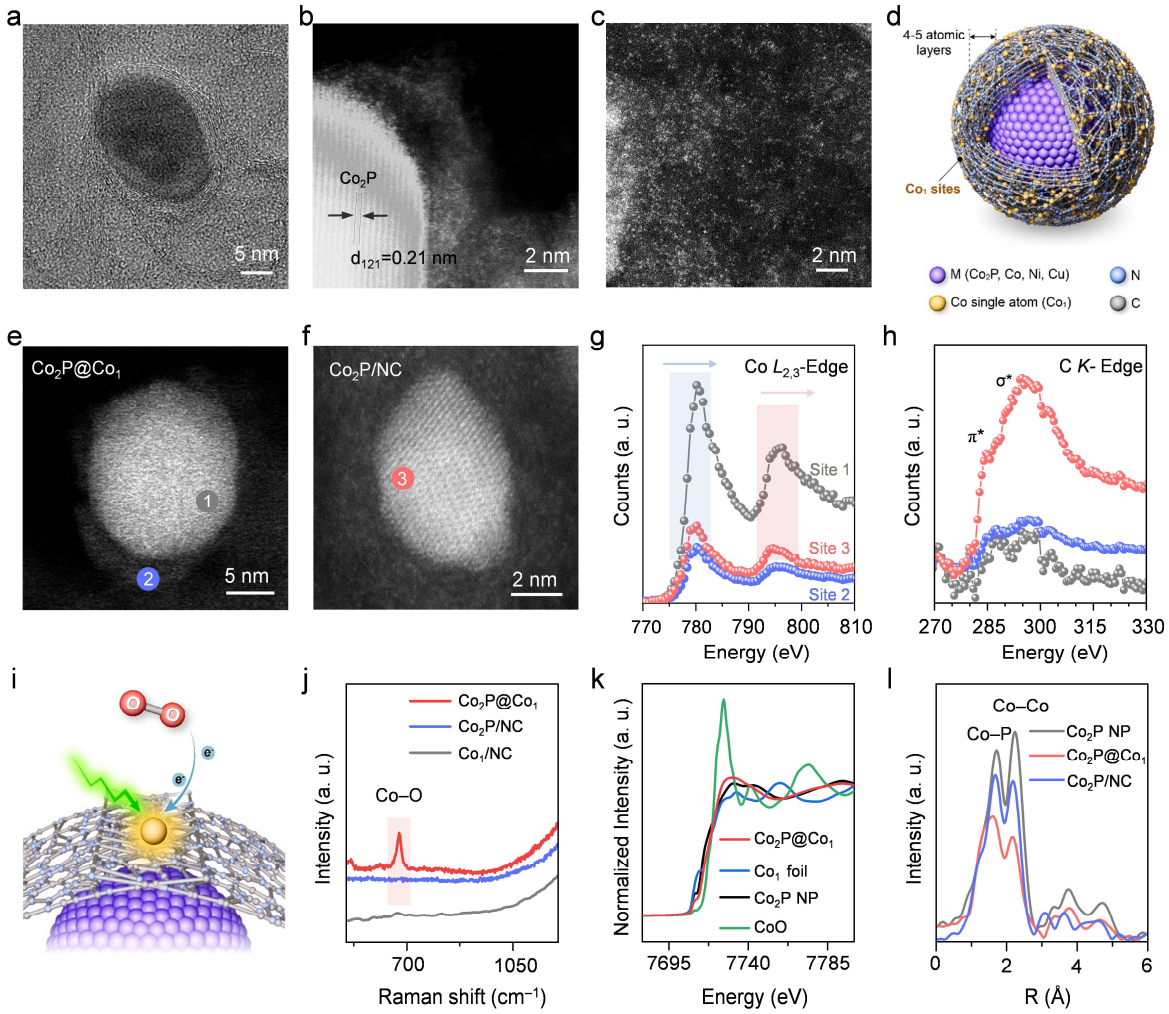
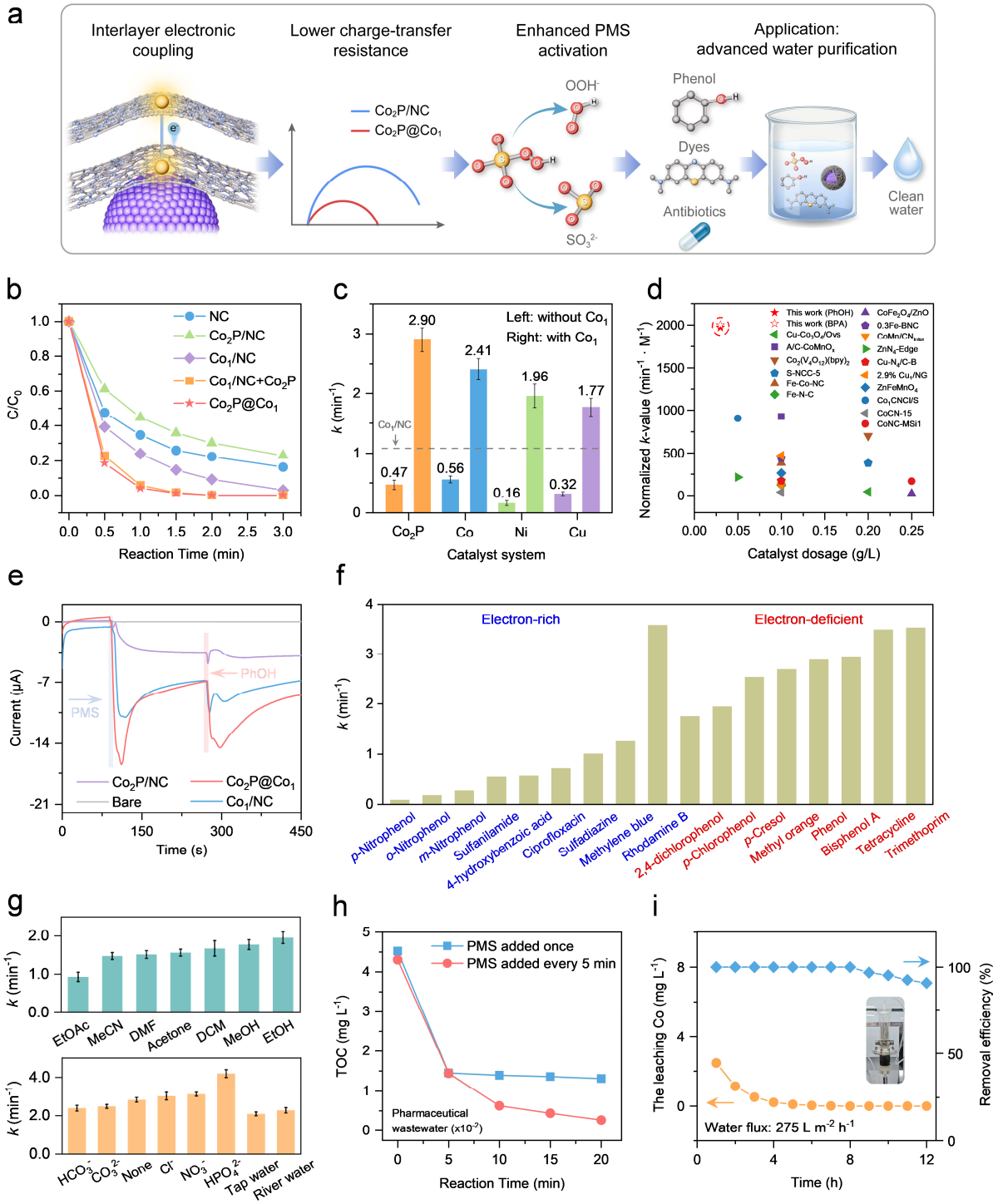


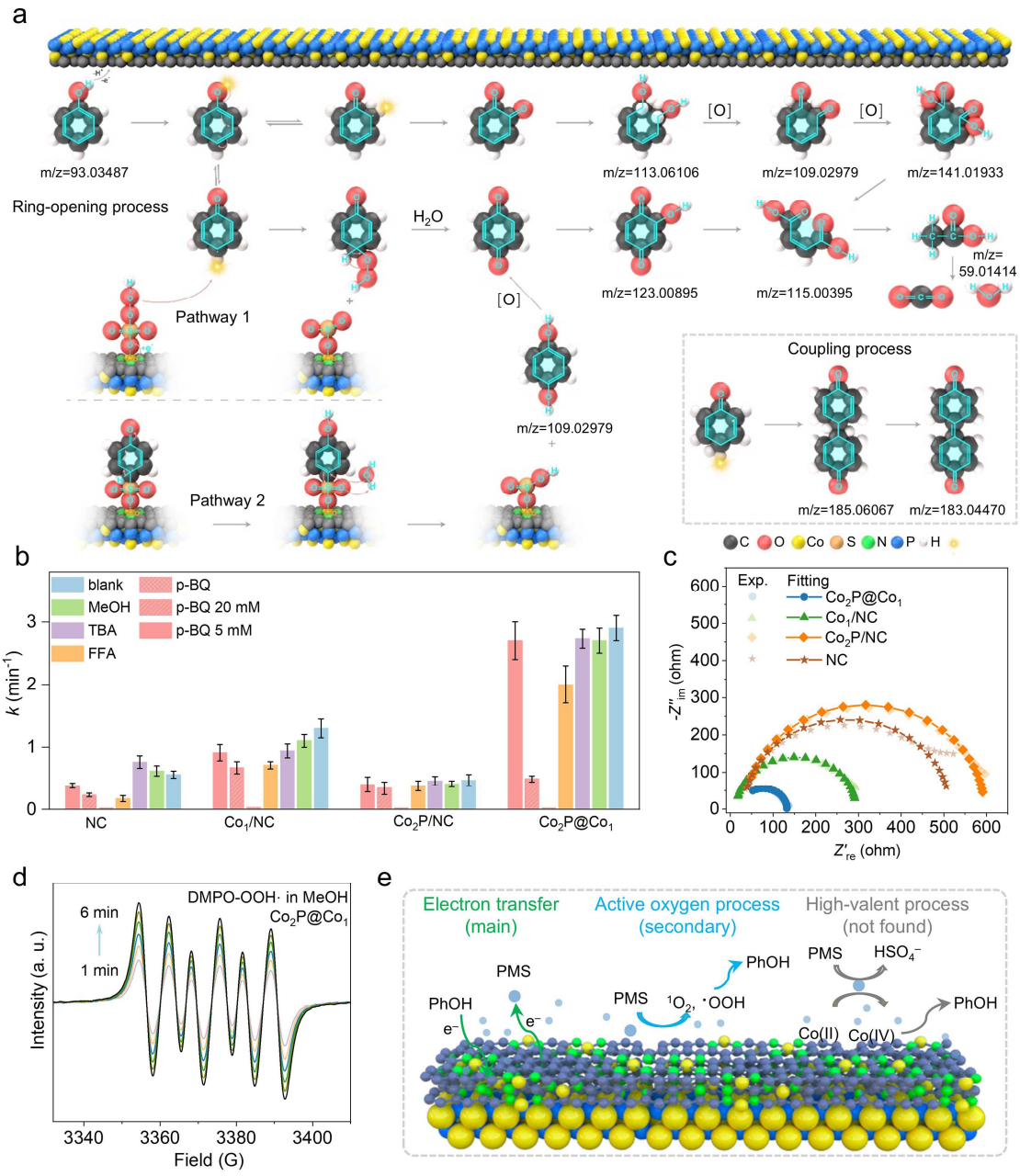
Fig. 1. Structure characterization of catalysts. (a) BF-HRTEM, (b) HAADF-STEM, (c) HAADF-STEM image highlighting the single-atom region image and (d) structure diagram of $Co_2P@Co_1$. HAADF-STEM images of (e) $Co_2P@Co_1$ and (f) Co_2P/NC with marked points for EELS analysis. Corresponding EELS spectra of (g) Co *L*-edge and (h) C *K*-edge acquired from the marked points in (e) and (f). (i) Raman schematic diagram and (j) its spectra acquired under ambient conditions with a 532-nm laser. (k) XANES spectra. (l) EXAFS spectra.



552

553 **Fig. 2. Catalytic performance for Fenton-like reactions.** (a) Schematic illustration of the
554 interlayer electronic coupling in Co_2P/NC. (b) degradation kinetics of PhOH over different
555 catalyst systems. (c) Apparent pseudo-first-order rate constants (k) for PhOH degradation over

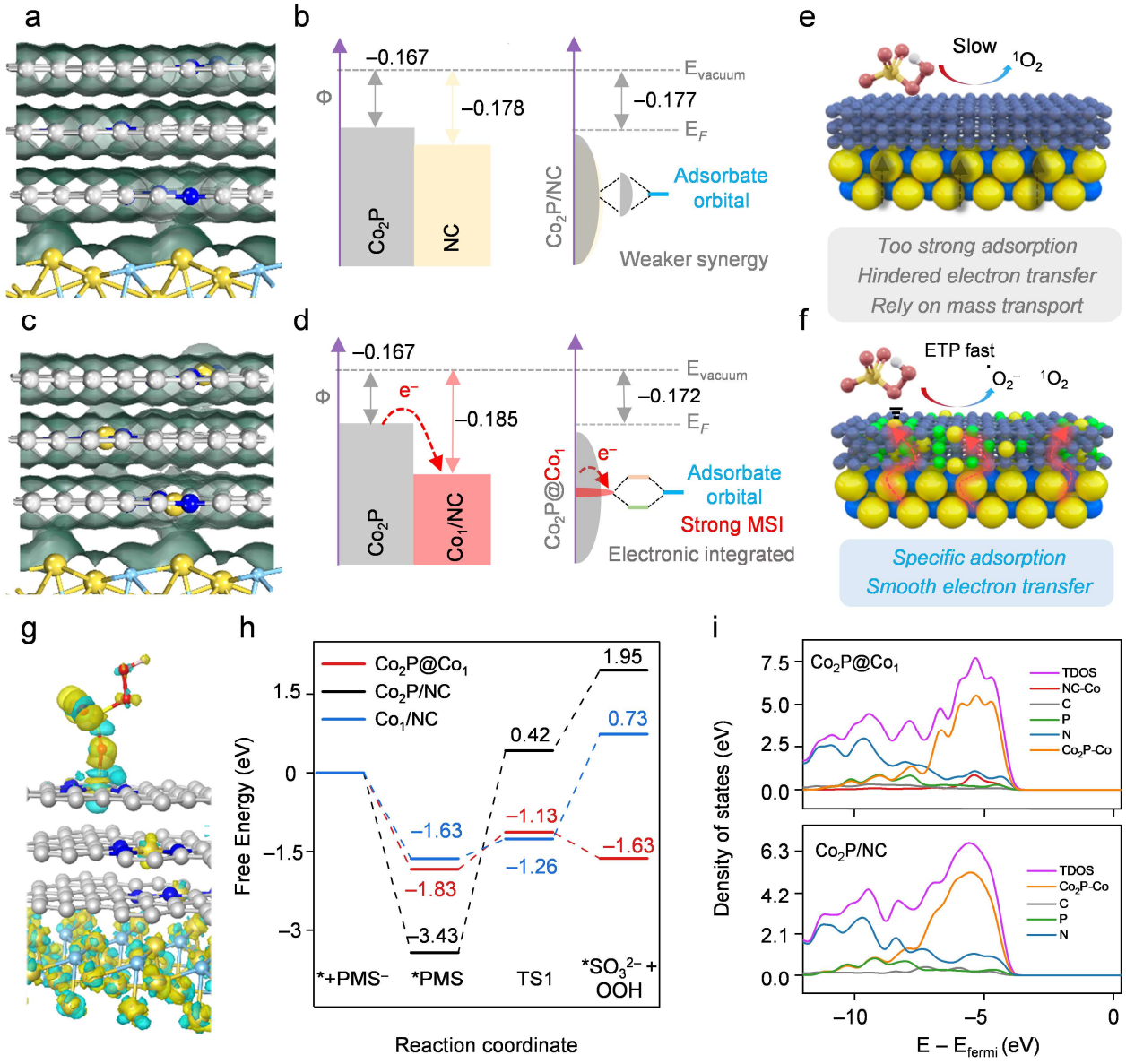
Co_2P-, Co-, Ni- and Cu-based catalyst systems in the absence and presence of Co_1. (d) Comparison of the normalized degradation rate constants and catalyst dosages of the developed catalyst with previously reported systems. (e) Chronoamperometric response upon the addition of PMS and phenol. (f) Degradation performance for various pollutants. (g) *k* values under interference from different solvents (10 vol% in water) and various anions. (h) Total organic carbon (TOC) removal during pharmaceutical wastewater treatment under single-dose and repeated PMS addition conditions. (i) Catalyst performance stability in a flow-through system.



564

565 **Fig. 3. Mechanism of phenol degradation.** (a) Proposed phenol degradation pathway over the
566 $Co_2P@Co_1$ catalyst based on mass spectrometry fragments. (b) Quenching effects of different
567 scavengers. (Unless otherwise stated, the concentration of scavengers is 50 mM) (c)
568 Electrochemical impedance spectroscopy (EIS) plots of $Co_2P@Co_1$ and control catalysts. (d) In-
569 situ electron paramagnetic resonance (EPR) spectra for superoxide radical detection. (e)
570 Schematic illustration of the proposed phenol degradation mechanism over the $Co_2P@Co_1$
571 catalyst.

572



573

574 **Fig. 4. Theoretical analysis of the enhanced electron transfer mechanism**. Electron density
575 distribution of (a) Co_2P/NC and (c) Co_2P@Co_1. Isosurface value: 0.13989. Work function
576 analysis of (b) Co_2P/NC and (d) Co_2P@Co_1. Schematic illustration of charge transfer capability
577 for (e) Co_2P/NC and (f) Co_2P@Co_1. (g) Difference charge density for PMS adsorption on
578 Co_2P@Co_1. (h) Free energy diagram for PMS activation via the superoxide pathway. (i) Density
579 of states (DOS) analysis.

Supplementary Files

This is a list of supplementary files associated with this preprint. Click to download.

- SupplementaryInformation.pdf